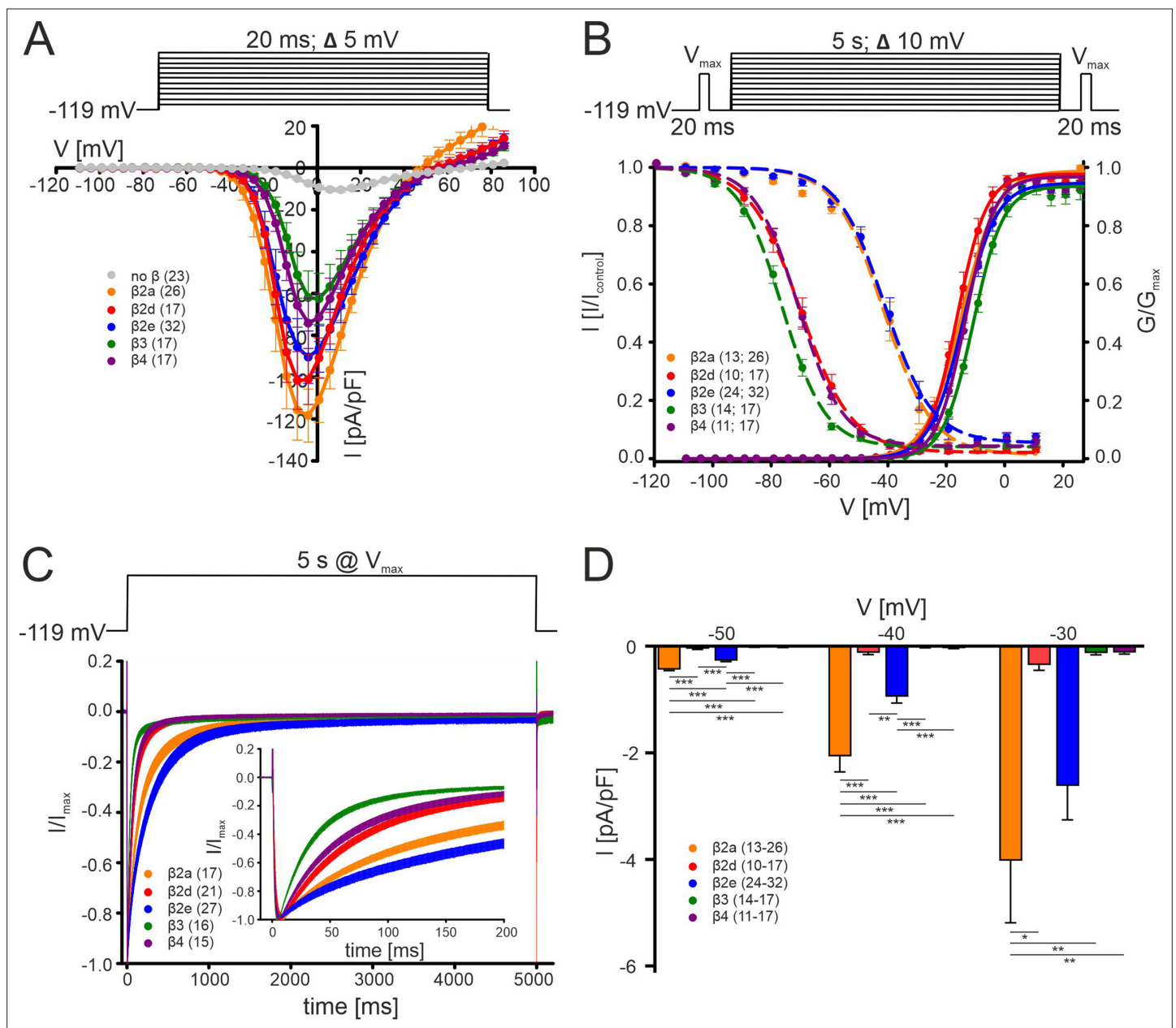


---

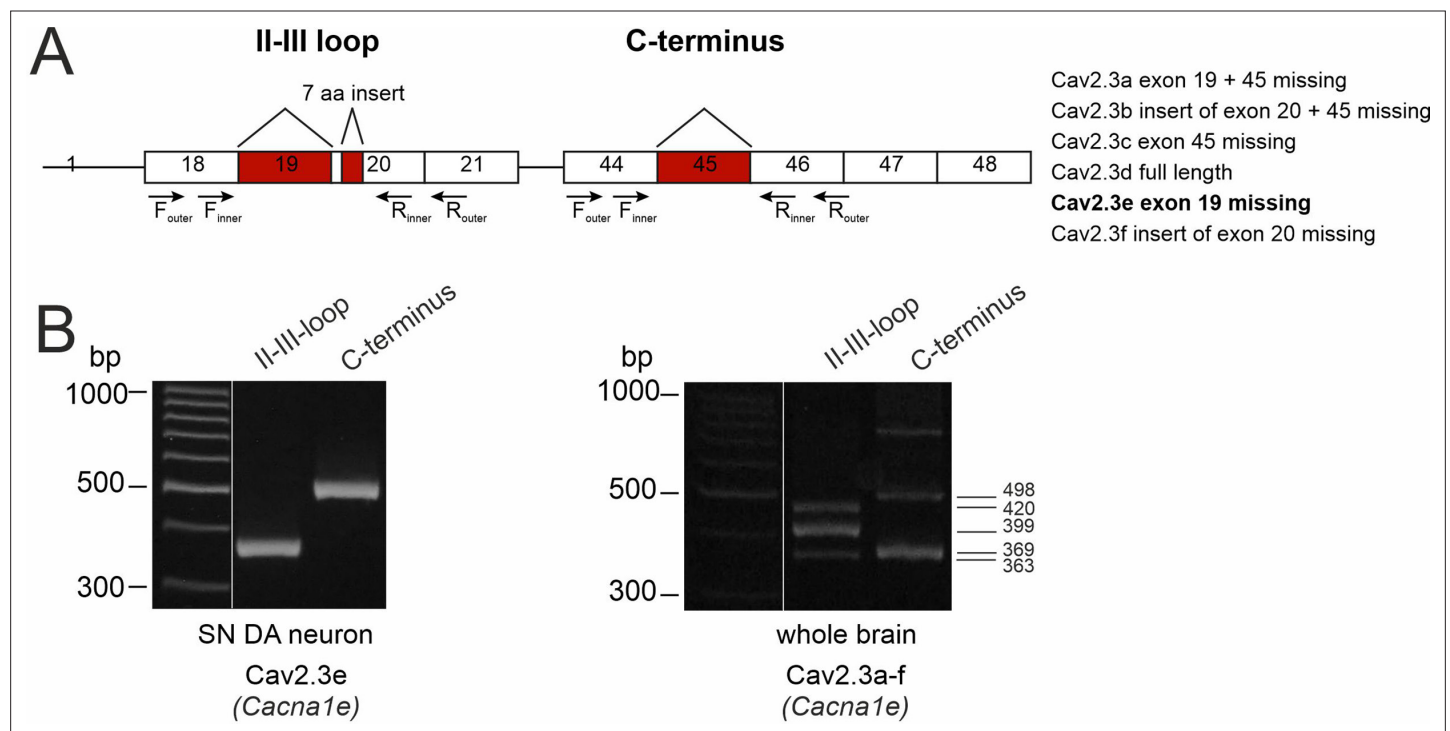
## Figures and figure supplements

$\beta$ 2-subunit alternative splicing stabilizes Cav2.3  $\text{Ca}^{2+}$  channel activity during continuous midbrain dopamine neuron-like activity

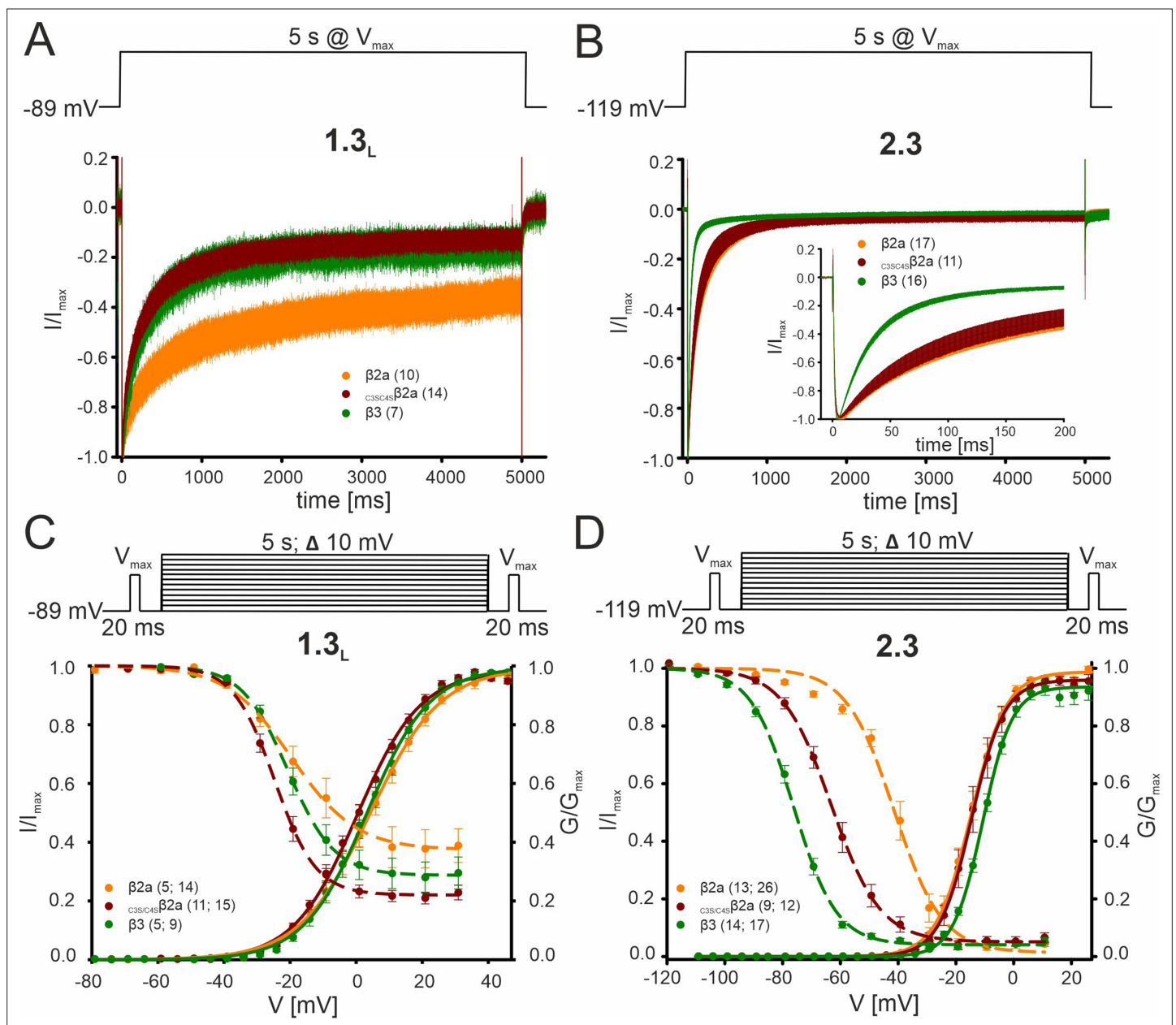
**Anita Siller et al**



**Figure 1.** Biophysical properties of Cav2.3 channels co-transfected with different  $\beta$ -subunits (and  $\alpha$ 2 $\delta$ 1) in tsA-201 cells. **(A)** Current densities (pA/pF) with or without (gray) co-transfection of indicated  $\beta$ -subunits. Color code and n-numbers are given in the graphs. **(B)** Voltage-dependence of steady-state activation (normalized conductance  $G$ , right axis, solid lines) and inactivation (normalized  $I_{Ca}$  of test pulses, left axis, dashed lines, left n-numbers in parentheses). **(C)** Inactivation time course during 5 s depolarizing pulses to  $V_{max}$  starting from a holding potential of  $-119$  mV. Inset shows the first 200 ms of the 5 s pulse. The curves represent the means  $\pm$  SEM for the indicated number of experiments ( $N = \beta$ 2a: 5;  $\beta$ 2d,  $\beta$ 2e: 2;  $\beta$ 3,  $\beta$ 4, no  $\beta$ : 3). For statistics see **Table 1**.  $V_{max}$ , voltage of maximal inward current. **(D)** Window currents measured in the presence of the indicated  $\beta$ -subunits were calculated by multiplying mean current densities (pA/pF) of I-V-relationships by the fractional current inactivation from steady-state inactivation curves at the indicated voltages. Data represent the means  $\pm$  SEM for the indicated number of experiments ( $N = \beta$ 2a: 5;  $\beta$ 2d,  $\beta$ 2e: 2;  $\beta$ 3,  $\beta$ 4: 3). Statistical significance was determined using one-way ANOVA with Bonferroni post-hoc test and is indicated: \*\*\*  $p < 0.001$ ; \*\*  $p < 0.01$ ; \*  $p < 0.05$ . Source data provided in **Figure 1—source data 1**.



**Figure 1—figure supplement 1.** Determination of the expressed Cav2.3 splice variants in SN DA neurons. **(A)** Cartoon of the exon structure of all Cav2.3 splice variants. The murine *Cacna1e* gene, coding for the Cav2.3  $\alpha 1$ -subunits contains 48 exons with six major alternative splice variants (right panel). The splicing events include the variable use of exon 19, 21 nucleotides of exon 20 and exon 45. The outer and inner primer pairs chosen for identification of the different splice variants are located in the II-III loop and the C-terminus, covering the three described splicing sites. Expressed exons are shown as white boxes and splicing sites are indicated in red. **(B)** Agarose gel electrophoresis image showing two PCR products (363 bp II-III loop nested PCR fragment and 498 bp C-terminus nested PCR fragment) coding for the Cav2.3e splice variant of Cav2.3 (*Cacna1e*) found in mouse laser-dissected SN DA neuron derived cDNA ( $n=40$ , left). In contrast, all five PCR products (363 bp, 399 bp, and 420 bp in the II-III loop and 369 bp and 498 bp in the C-terminus nested PCR fragments) coding for all six major splice variants were found in whole brain tissue-derived cDNA (as positive control, right panel).



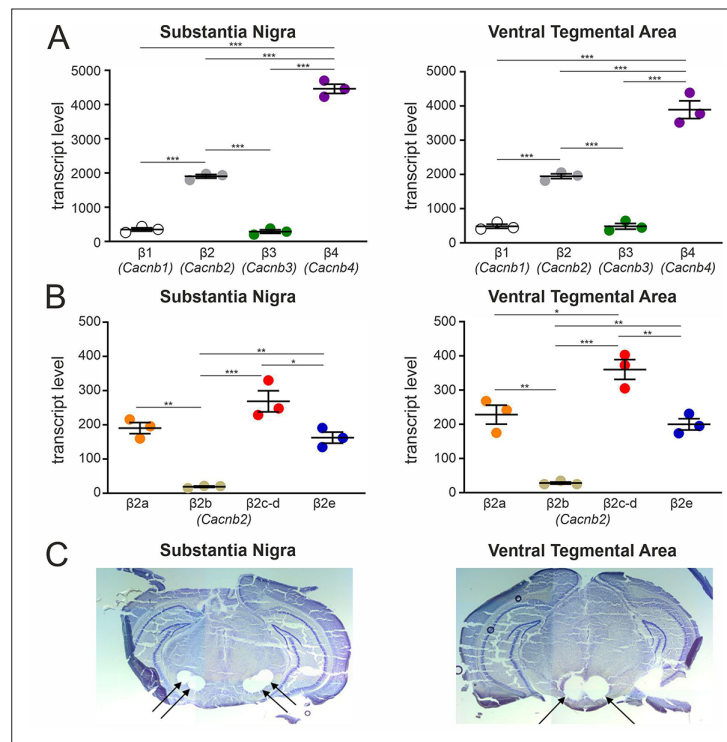
**Figure 1—figure supplement 2.** Effect of  $\beta 2a$  palmitoylation on the biophysical properties of Cav2.3 and Cav1.3  $Ca^{2+}$  channels in tsA-201 cells. Since palmitoylation is reversible and regulated in an activity-dependent localized manner (Bijlmakers and Marsh, 2003; Matt et al., 2019), we also investigated the contribution of palmitoylation of  $\beta 2a$  for Cav2.3e modulation under our experimental conditions. To mimic the de-palmitoylated form, we replaced the two N-terminal cysteines to serines ( $C3S/C4S\beta 2a$ ) which prevents plasma membrane anchoring of  $\beta 2a$  (Gebhart et al., 2010; Qin et al., 1998). Data are shown for Cav1.3 (C-terminally long splice variant, Bock et al., 2011) or Cav2.3  $\alpha 1$ -subunits co-expressed with  $\alpha 2\delta 1$  and  $\beta 2a$  (orange),  $C3S/C4S\beta 2a$  (red) or  $\beta 3$  (green). Respective command voltages are given in each panel. To disrupt palmitoylation-mediated membrane anchoring, the two N-terminal cysteines of  $\beta 2a$  (see Figure 2—figure supplement 1) were replaced by serines in  $C3S/C4S\beta 2a$ . (A, B) Inactivation kinetics during a 5 s long depolarizing step to  $V_{max}$  for Cav1.3<sub>L</sub> (A), 15 mM  $Ca^{2+}$ , holding potential -89 mV or Cav2.3 (B), 2 mM  $Ca^{2+}$ , holding potential -119 mV. Curves represent means  $\pm$  SEM for the indicated number of experiments. For statistics see Table 1 and Supplementary file 6. (C, D) Voltage-dependence of activation (solid lines, normalized conductance  $G$ ) and inactivation (dashed lines, normalized  $I_{Ca}$  of 20-ms test pulses) for Cav1.3<sub>L</sub> (C) 15 mM  $Ca^{2+}$ , holding potential -89 mV or Cav2.3 (D), 2 mM  $Ca^{2+}$ , holding potential -119 mV. Means  $\pm$  SEM. For statistics see Table 1 and Supplementary file 6.  $C3S/C4S\beta 2a$  significantly shifted  $V_{0.5,inact}$  of Cav2.3 to more positive voltages as compared to  $\beta 3$  but to a much smaller extent (<14 mV) than  $\beta 2a$  (+35 mV) (Table 1). Due to this prominent role of palmitoylation on the  $V_{0.5,inact}$  of Cav2.3 channels, the palmitoylation state of  $\beta 2a$  should allow further fine-tuning of non-inactivating current components of Cav2.3 channels in SN DA neurons. The effects of  $\beta 2a$  palmitoylation on the inactivation kinetics and inactivation voltage of Cav1.3 L-type channels (A, C) were different from Cav2.3, suggesting that palmitoylation/depalmitoylation events would regulate  $Ca^{2+}$  channel function in a subtype-selective manner. Unlike  $\beta 2a$ ,  $C3S/C4S\beta 2a$  was unable to slow the inactivation time course of Cav1.3, thus stabilizing faster

Figure 1—figure supplement 2 continued on next page



*Figure 1—figure supplement 2 continued*

inactivation similar to  $\beta 3$  (**Supplementary file 6, Gebhart et al., 2010**). In contrast, preventing palmitoylation of  $\beta 2a$  did not affect the inactivation time course of Cav2.3e (**Table 1**). Moreover, unlike observed for Cav2.3, steady-state inactivation was not significantly different for Cav1.3 co-transfected with  $\beta 2a$ ,  $\beta 3$ , or  $C_{35/C45}\beta 2a$  (**Supplementary file 6**). Source data provided in **Figure 1—figure supplement 2—source data 1**.



**Figure 2.** Transcript expression of various  $\beta$ -subunits and  $\beta2$ -subunit splice variants in mouse SN and VTA tissue. (A) Expression of  $\beta1$ - $\beta4$  subunit transcripts in SN (n=3, N=3) (left) and VTA (n=3, N=3) (right) determined by RT-qPCR as described in Methods. (B) Expression of  $\beta2a$ - $\beta2e$  subunit transcripts in SN (n=3, N=3) (left) and VTA (n=3, N=3) (right). Data are shown as the mean  $\pm$  SEM. Statistical significance was determined using one-way ANOVA followed by Bonferroni post-hoc test: \*\*\*  $p < 0.001$ ; \*  $p < 0.01$ ; \*  $p < 0.05$ . Data was normalized to Gapdh and Tfric determined by geNorm. (C) Example for four SN (left) and two VTA (right) tissue punches obtained for cDNA preparation with diameters of 0.5 mm each (left) or 0.8 mm each (right) from 7 to 8 successive 100- $\mu$ m-sections between Bregma  $-3.00$  mm and  $-3.80$  mm, stained with Cresyl violet. Source data provided in **Figure 2—source data 1**.

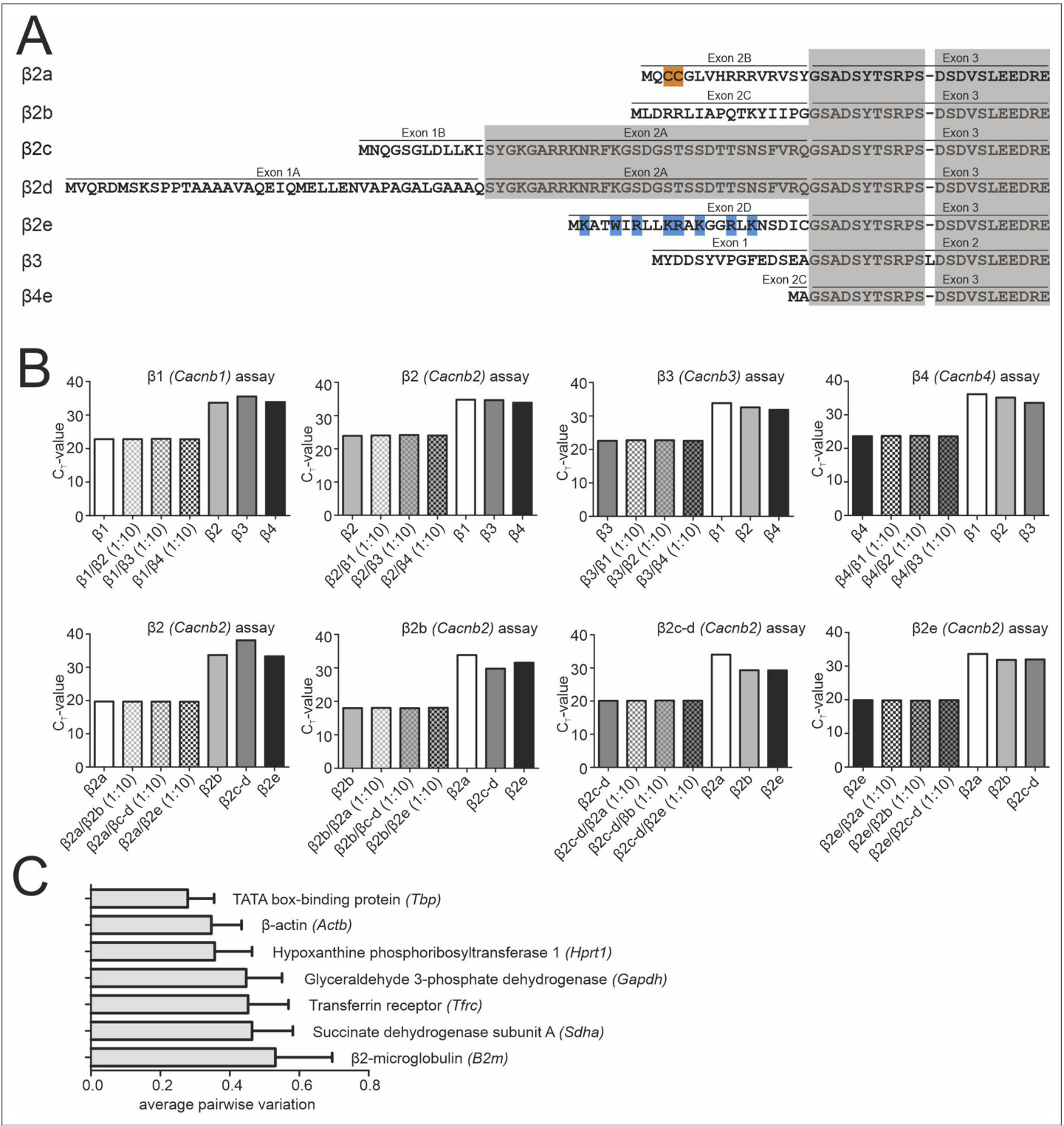


**Figure 2—figure supplement 1.** Binding specificity of β1-β4 and β2a-β2e TaqMan assays and expression stability of endogenous control genes. (A) Alignment of the N-terminal amino acid sequence of the investigated β-subunits (β2a, β2d, β2e, β3, or β4). Residues responsible for membrane anchoring of β2a (palmitoylated cysteine residues are highlighted in orange) and β2e (positively charged amino acids forming a lipid binding motif are highlighted in blue) are indicated. Homologous exons are shaded in gray. Sequence accession numbers (human CACNB2 (β2) splice variants): β2a (NP\_000715.2), β2d (NP\_963887.2), β2e (NP\_963864.1), β3 (NP\_000716.2), β4e (NP\_001307651.1). (B) The indicated β-subunit isoforms (β1-β4; n=3; gene names in parenthesis) and β2 splice variants (n=3) were recognized with high specificity (low CT value) by the corresponding RT-qPCR assay even in the presence of a 10-fold higher concentration of the mismatching DNA fragments corresponding to other isoforms/splice variants (β1-4: Figure 2—figure supplement 1 continued on next page

*Figure 2—figure supplement 1 continued*

n=1;  $\beta$ 2 splice variants: n=1). High binding specificity was confirmed by inefficient detection (high CT value) of all non-matching DNA fragments. We additionally performed experiments with a mixture of the specific with mismatching  $\beta$ -subunit DNA at ratios of 1:1, 1:2, and 1:5, and only the 1:10 mix is shown (similar CT values for all combinations). (C) Average expression stability of endogenous control genes in SN and VTA tissue. All reference genes maintained comparable cDNA concentrations throughout the experiments. Data were normalized to the expression of Glyceraldehyde 3-phosphate dehydrogenase (Gapdh) and Transferrin receptor (Tfrc) determined by geNorm. Data are given as means  $\pm$  SEM (n=6, N=6). Source data provided in

**Figure 2—figure supplement 1—source data 1.**

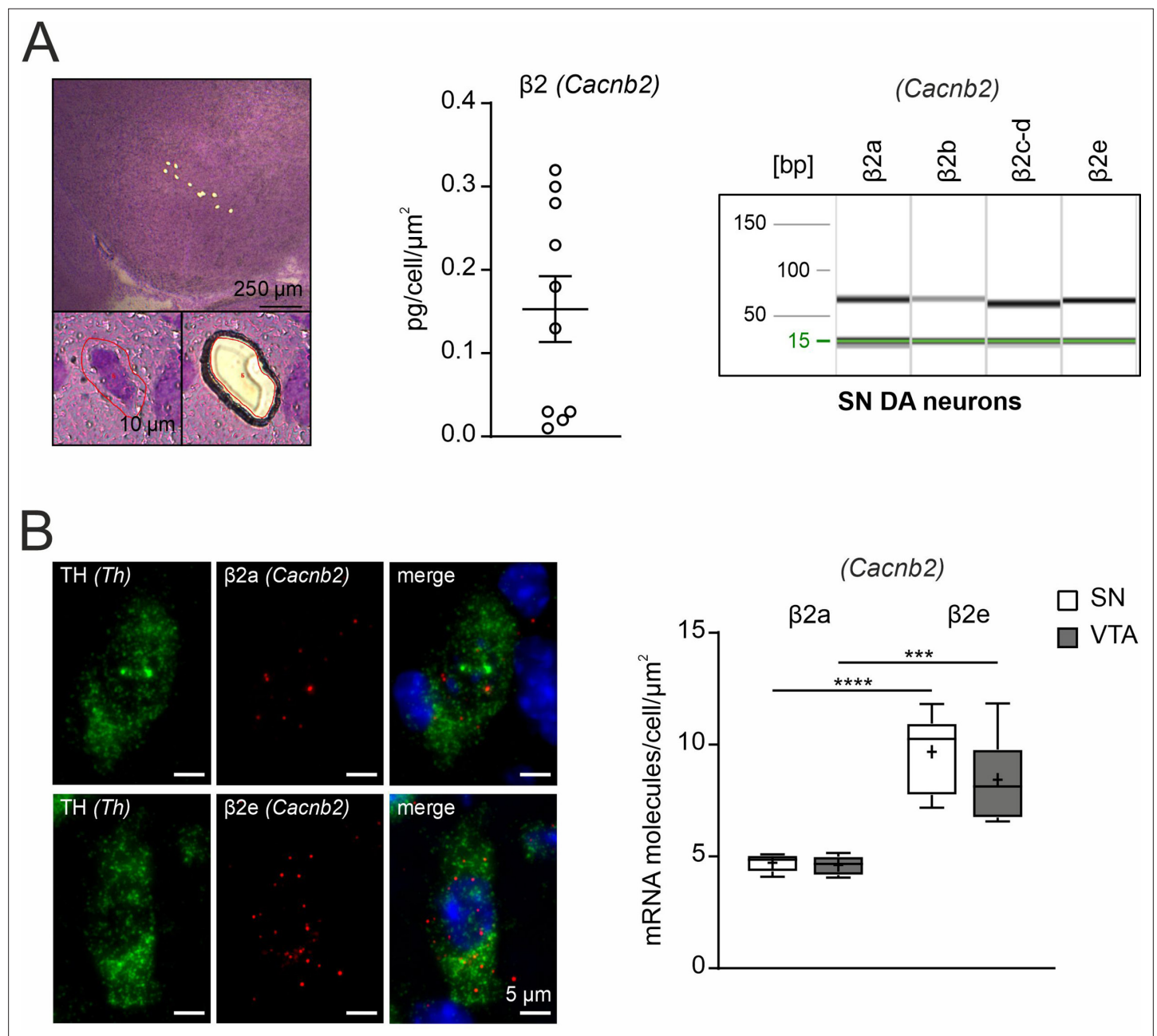


**Figure 2—figure supplement 2.** Expression of  $\beta 2$ -subunit splice variants in UV-LMD SN DA neurons. **(A)** Left: Overview of a cresyl violet (CV) stained coronal midbrain section of a juvenile wildtype mouse after UV-LMD of 10 SN DA neurons (scale bar: 250  $\mu\text{m}$ , upper). Image of one CV stained SN DA neuron of a juvenile wildtype mouse before and after UV-LMD (scale bar: 10  $\mu\text{m}$ , lower). Middle:  $\beta 2$ -subunit transcript relative mRNA quantification by reverse transcription quantitative PCR-based in UV-LMD mouse SN DA neurons ( $n=10$ ). Right: Capillary gel electrophoresis image illustrating PCR products of  $\beta 2$ -subunit (*Cacnb2*) splice variants amplified from a UV-LMD cDNA template corresponding to 2.9 cells. **(B)** Left: Representative images showing  $\beta 2a$  and  $\beta 2e$  (red) or tyrosine hydroxylase (TH) (*Th*), green) RNAscope fluorescence signals (combined with nuclear DAPI staining, blue) of individual SN DA neurons from an adult wildtype mouse. Scale bar: 5  $\mu\text{m}$ . Right: Absolute mRNA transcript numbers per cell for  $\beta 2$  (*Cacnb2*) - variants  $\beta 2a$  or  $\beta 2e$  in adult SN DA and VTA DA neurons of adult wildtype mice ( $N=6$ , each), as indicated. Tukey's boxplots are shown. Significances are indicated by asterisks: \*\*\*  $p<0.001$ , \*\*\*\*  $p<0.0001$ . For statistics see details in **Supplementary file 4**. Source data provided in **Figure 2—figure supplement 2—source data 1**.

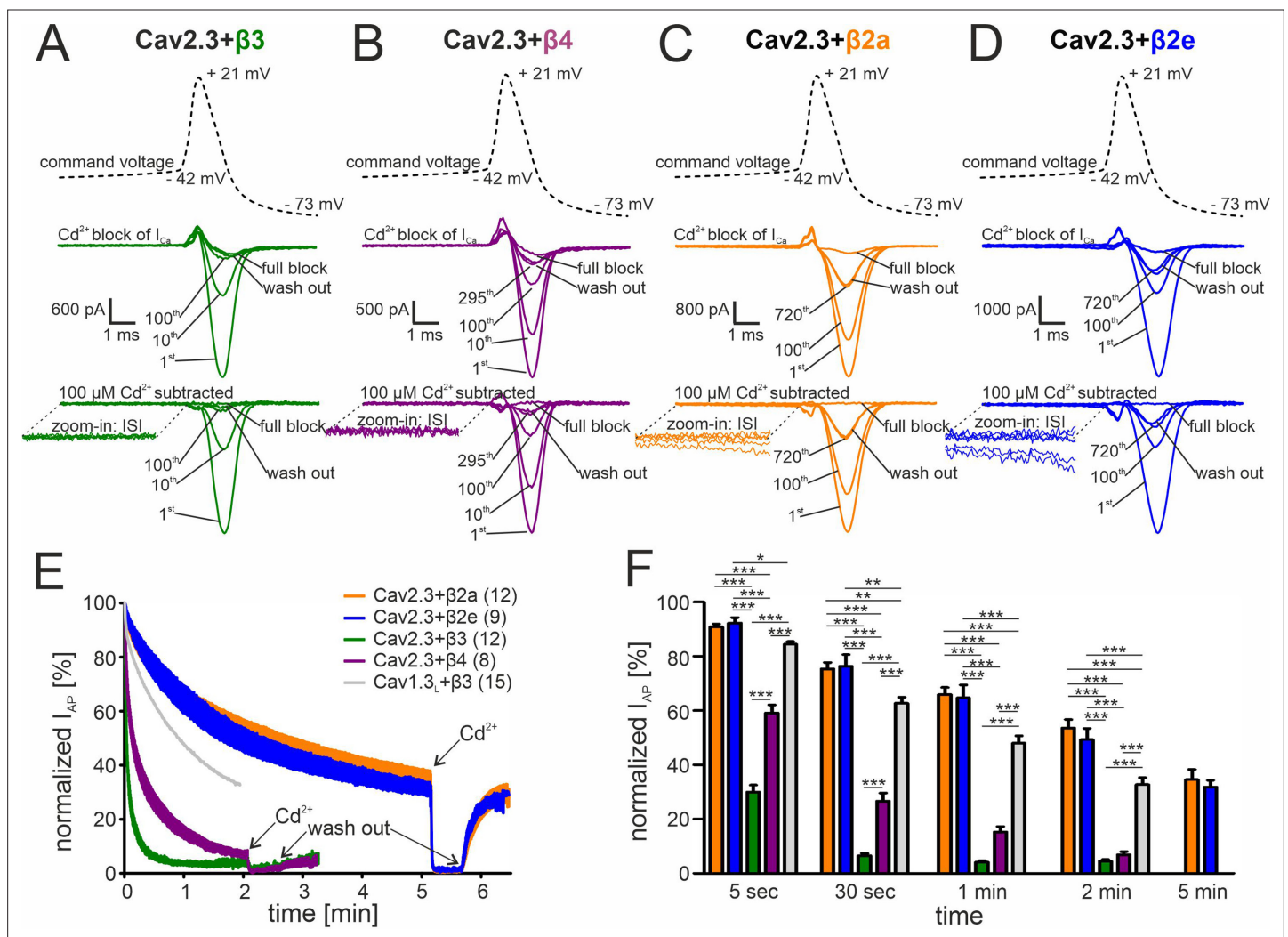


**Figure 3.** Activity-dependent inactivation of Cav2.3 channels co-transfected with different  $\beta$  subunits (and  $\alpha 2\delta 1$ ) during simulated SN DA neuron regular pacemaking activity in tsA-201 cells. **(A–D)** Top panel: The SN DA neuron-derived command voltage was applied with a frequency of 2.5 Hz (only a time interval around the AP-spike is shown). Middle panel: Corresponding representative  $\text{Ca}^{2+}$  current traces (2 mM charge carrier) for Cav2.3 channels co-expressed with  $\alpha 2\delta 1$  and  $\beta 3$  (A, green),  $\beta 4$  (B, purple),  $\beta 2a$  (C, orange), or  $\beta 2e$  (D, blue) are shown for the indicated sweep number (1st, 10th, 100th, 295th, 720th). Cav2.3 currents were completely blocked by 100  $\mu\text{M}$  Cadmium ( $\text{Cd}^{2+}$ ), and remaining  $\text{Cd}^{2+}$ -insensitive current components were subtracted off-line (bottom panel). ISI, interspike interval. **(E)** Current decay during simulated 2.5 Hz SN DA neuron pacemaking. Normalized peak inward current during APs ( $I_{\text{AP}}$ ) is plotted against time as mean  $\pm$  SEM for the indicated number of experiments.  $I_{\text{AP}}$  amplitudes were normalized to the  $I_{\text{AP}}$  amplitude of the first AP after holding the cell at  $-89$  mV. Cav1.3 $_L$  co-expressed with  $\alpha 2\delta 1$  and  $\beta 3$  (gray, mean only) is shown for comparison (data taken from [Ortner et al., 2017](#)). The  $I_{\text{AP}}$  decay was fitted to a bi-exponential function (Cav2.3  $\beta 3$ :  $A_{\text{slow}} = 39.4\% \pm 0.65\%$ ,  $\tau_{\text{slow}} = 22.2 \pm 0.15$  min,  $A_{\text{fast}} = 54.2 \pm 0.76\%$ ,  $\tau_{\text{fast}} = 2.86 \pm 0.07$  min, non-inactivating =  $4.47\% \pm 0.13\%$ ;  $\beta 4$ :  $A_{\text{slow}} = 48.5 \pm 0.26\%$ ,  $\tau_{\text{slow}} = 90.3 \pm 1.07$  min,  $A_{\text{fast}} = 41.8 \pm 0.40\%$ ,  $\tau_{\text{fast}} = 8.39 \pm 0.16$  min, non-inactivating =  $5.12\% \pm 0.12\%$ ;  $\beta 2a$ :  $A_{\text{slow}} = 52.6 \pm 0.47\%$ ,  $\tau_{\text{slow}} = 299.3 \pm 10.2$  min,  $A_{\text{fast}} = 13.4 \pm 0.53\%$ ,  $\tau_{\text{fast}} = 18.2 \pm 1.47$  min, non-inactivating =  $32.3\% \pm 0.77\%$ ;  $\beta 2e$ :  $A_{\text{slow}} = 67.7 \pm 0.11\%$ ,  $\tau_{\text{slow}} = 294.1 \pm 1.77$  min,  $A_{\text{fast}} = 7.10 \pm 0.27\%$ ,  $\tau_{\text{fast}} = 16.6 \pm 1.24$  min, non-inactivating =  $25.0\% \pm 0.12\%$ ). Curves represent the means  $\pm$  SEM for the indicated number of experiments (independent transfections, N=Cav2.3/ $\beta 3$ : 4; Cav2.3/ $\beta 4$ : 2; Cav2.3/ $\beta 2a$ : 4; Cav2.3/ $\beta 2e$ : 2; Cav1.3 $_L$ / $\beta 3$ : 6). **(F)** Normalized  $I_{\text{AP}}$  decay after predefined time points for Cav2.3 with  $\beta 3$ ,  $\beta 4$ ,  $\beta 2a$  or  $\beta 2e$ , and Cav1.3 $_L$  (with  $\beta 3$ ). Color-code and n-numbers as in panel E. Statistical significance was determined using one-way ANOVA followed by Bonferroni post-hoc test: \*\*\*  $p < 0.001$ ; \*\*  $p < 0.01$ ; \*  $p < 0.05$ . Source data provided in [Figure 3—source data 1](#).



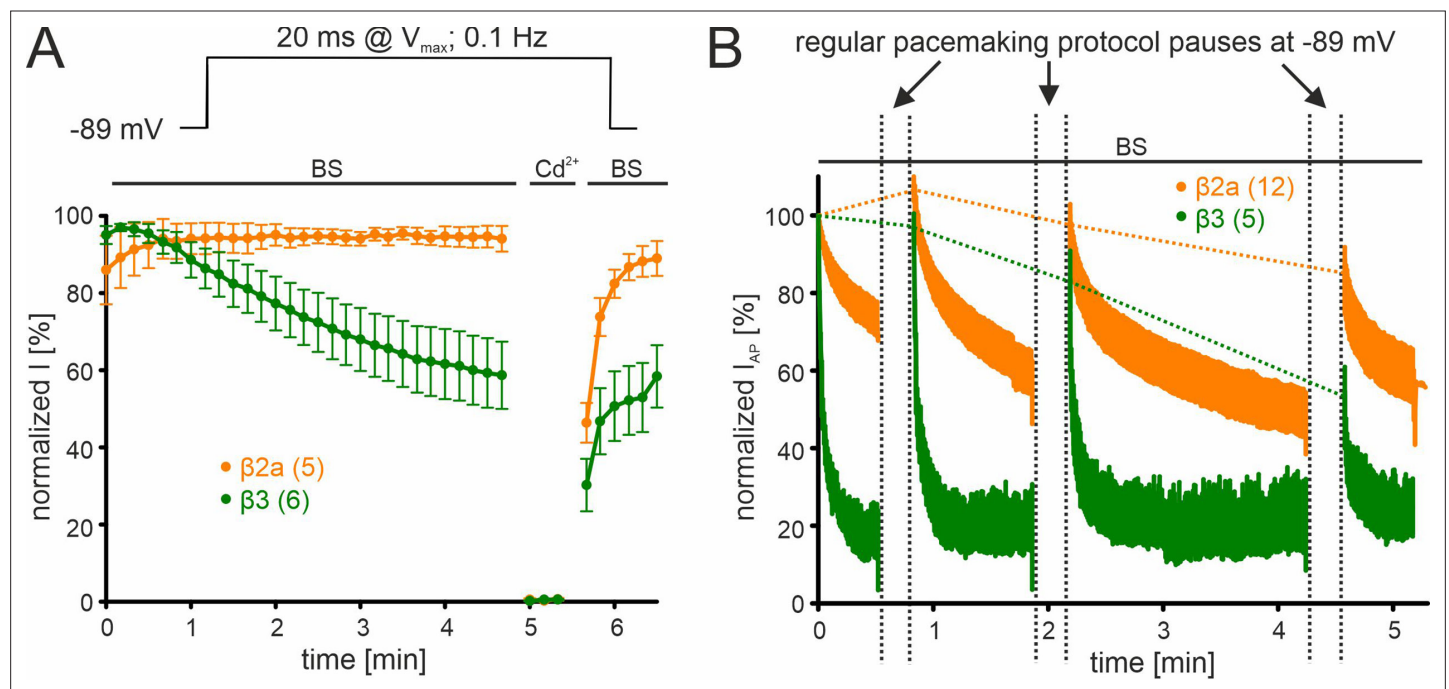


**Figure 4.**  $\beta$ -subunit-dependent run-down of Cav2.3 channel  $Ca^{2+}$  current in tsA-201 cells. Data for Cav2.3 co-expressed with  $\alpha 2\delta 1$  and  $\beta 2a$  (orange) or  $\beta 3$  (green) are shown. **(A)** Run-down during a 0.1 Hz square pulse protocol (20 ms to  $V_{max}$ , holding potential -89 mV). Currents were normalized to the  $I_{Ca}$  of the sweep with the maximal peak inward current observed during the recording. After a full block with 100  $\mu M$   $Cd^{2+}$  currents recovered to the amplitude preceding the  $Cd^{2+}$  application. **(B)** Cells were held at -89 mV and then stimulated using the regular SN DA neuron pacemaking protocol for 30 s, 1 min, and 2 min each followed by 20 s long pauses (vertical dashed lines) at hyperpolarized potentials (-89 mV) to allow channel recovery from inactivation.  $I_{AP}$  of individual APs was normalized to the inward current of the first AP. The current run-down component can be estimated from the non-recovering current component (horizontal dashed lines). Traces represent means  $\pm$  SEM from the indicated number of experiments ( $N=2$ ). BS, bath solution.

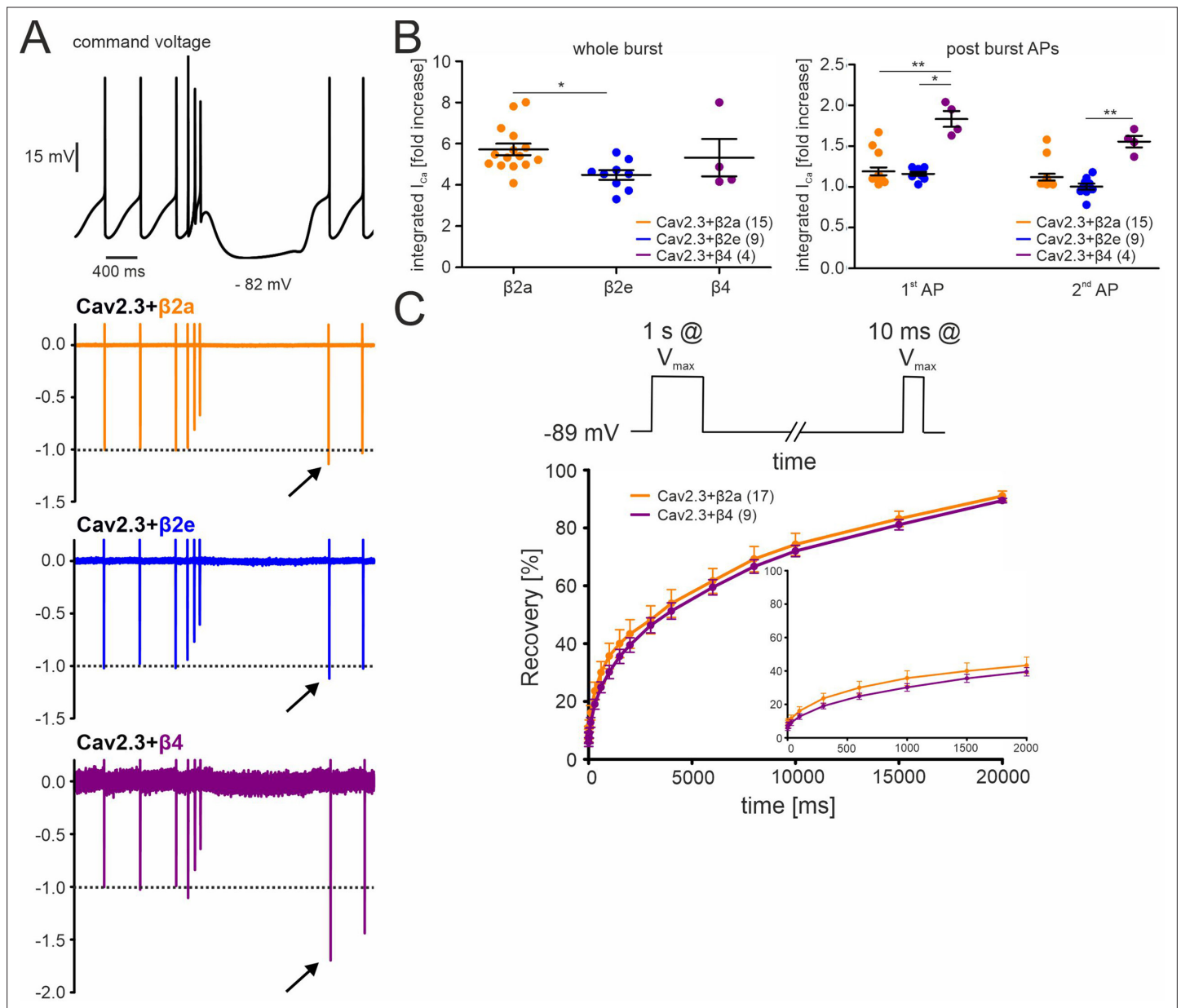


**Figure 5.** Effects of different  $\beta$ -subunits on Cav2.3 currents during a simulated SN DA neuron three-spike burst and post-burst APs in tsA-201 cells. The burst command voltage was elicited after ~5–6 min ( $\beta$ 2a,  $\beta$ 2e) or ~1–2 min ( $\beta$ 4) of regular pacemaking to reach steady-state  $I_{AP}$  ( $\beta$ 2a and  $\beta$ 2e: ~30% of the initial  $I_{AP}$ ;  $\beta$ 4: ~6% of the initial  $I_{AP}$ , see **Figure 3**). **(A)** Normalized current responses of Cav2.3 channels co-expressed with  $\beta$ 2a,  $\beta$ 2e or  $\beta$ 4 subunits (and  $\alpha$ 2 $\delta$ 1) induced by a command voltage (top panel) simulating a typical three-spike burst followed by a hyperpolarization phase at hyperpolarized potentials (lowest voltage: -82 mV) for 1.5 seconds. Remaining  $Cd^{2+}$ -insensitive current components (100  $\mu$ M  $Cd^{2+}$ ) were subtracted off-line to extract pure Cav2.3 mediated  $I_{Ca}$ . One of at least four experiments with similar results is shown. **(B)** The integrated  $I_{Ca}$  during a single AP before the burst (obtained as the mean of the three preceding APs) was set to 100% and compared with  $I_{Ca}$  during the three-spike burst integrated over the time period equivalent to one AP (left) or the first APs after the pause (right). All investigated  $\beta$ -subunits resulted in increased integrated  $I_{Ca}$  during the burst. Data represent the means  $\pm$  SEM for the indicated number of experiments (N =  $\beta$ 2a: 4;  $\beta$ 2e: 2;  $\beta$ 4: 2). Statistical significance was determined using one-way ANOVA followed by Bonferroni post-test (whole burst) or Kruskal-Wallis followed by Dunn's multiple comparison test (post-burst APs): \*\*\*  $p < 0.001$ ; \*\*  $p < 0.01$ ; \*  $p < 0.05$ . **(C)** Square-pulse protocol (top) used to determine recovery from inactivation after the indicated time intervals for  $\beta$ 2a and  $\beta$ 4-associated Cav2.3 channels (see Materials and methods for details). Data represent the means  $\pm$  SEM for the indicated number of experiments (N=3). For statistics see **Table 2**. Source data provided in **Figure 5—source data 1**.

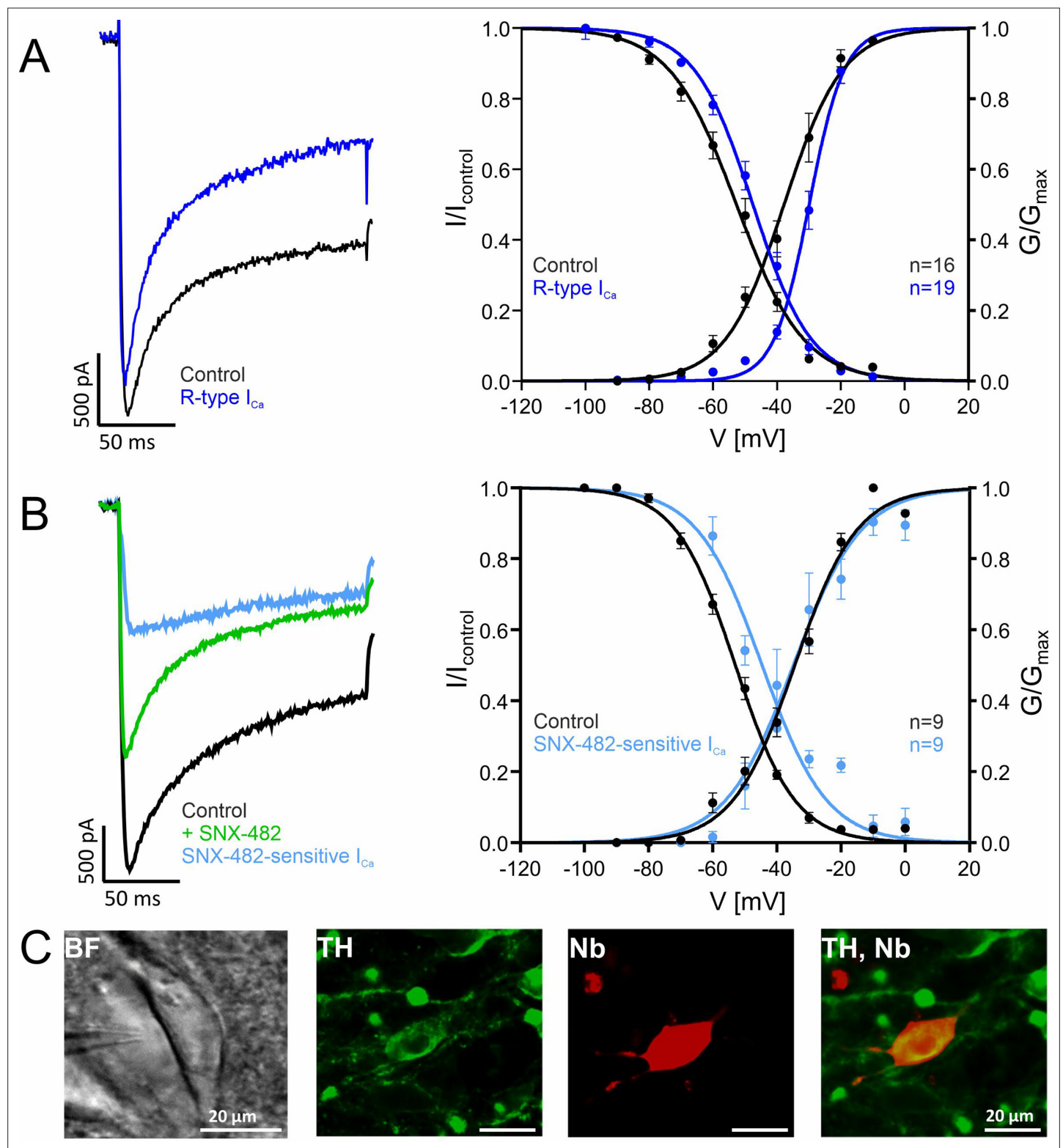


**Figure 6.** Voltage-dependence of gating of R-type currents in mouse SN DA neurons recorded in brain slices. **(A)**  $I_{Ca}$  recorded in SN DA neurons without (Control, black,  $n=16$ ) or after preincubation ("R-type", blue,  $n=19$ ) of slices with a Cav channel blocker cocktail to inhibit Cav3 (10  $\mu$ M Z941), Cav1 (1  $\mu$ M I), Cav2.1 and Cav2.2 (1  $\mu$ M  $\omega$ -conotoxin-MV1C) (see Methods). Left panel: representative current traces of recordings at  $-20$  mV test potentials (holding potential  $-100$  mV); notice that similar amplitudes of control and R-type current were chosen to facilitate comparison of current kinetics. Right panel: voltage-dependence of steady-state activation and inactivation, curve fits to a Boltzmann equation of all individual data points are shown. Data Figure 6 continued on next page

*Figure 6 continued*

are means  $\pm$  SEM. For parameters and statistics see **Table 3. (B)**. SNX-482-sensitive currents (light blue) were obtained by subtracting current measured in the presence of SNX-482 (green) from the respective control  $I_{Ca}$  before addition of SNX-482 (black) ( $n=9$ ). Left panel: Representative recording of a SNX-482 sensitive current component compared to the respective control (holding potential  $-100$  mV,  $-10$  mV test potential). Steady-state activation and inactivation of control and SNX-482-sensitive current. Test protocols: holding potential  $-100$  mV; voltage-dependence of activation: 150 ms test potentials to indicated voltages; voltage-dependence of inactivation: 5 s conditioning pulses to indicated voltages preceded ( $I_{control}$ ) and followed by 20 ms test pulses to  $V_{max}$ . **(C)** Exemplary neuron as seen under the patch-clamp microscope with patch pipette next to it (left; BF, brightfield) and a neuron after histochemical staining for tyrosine hydroxylase (TH, green) and neurobiotin (Nb, red). Detailed parameters and statistics are given in **Table 3**. Source data provided in **Figure 6—source data 1**.

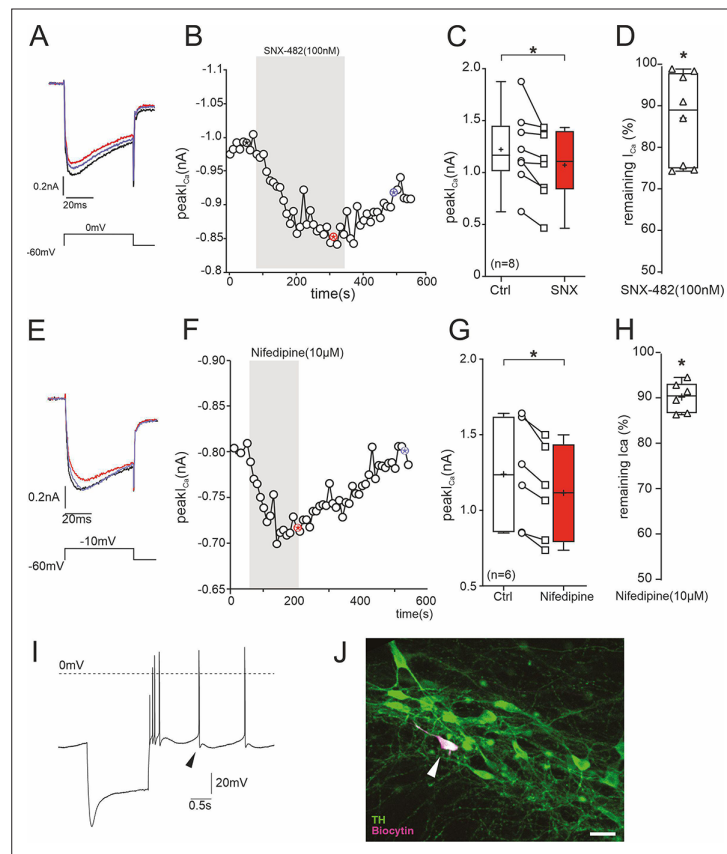


**Figure 6—figure supplement 1.** Inhibition of  $I_{Ca}$  in SN DA neurons of adult (12 weeks) mice by 100 nM SNX-482. To further prove the presence of SNX-482-sensitive R-type currents in SN DA neurons, we performed perforated-patch recordings. These allow stable recordings over a long period of time and to test for reversibility of channel block by 100 nM SNX-482. Recordings were performed with the pulse protocol shown in A (holding potential  $-60$  mV) after blocking  $I_A$   $K^+$ -currents known to be present in these cells to exclude block of  $I_A$  by SNX-482 (Kimm and Bean, 2014) as described previously (Benkert et al., 2019). 100 nM SNX-482 significantly reduced current to  $87\% \pm 4\%$  of control  $I_{Ca}$  ( $n=8$ ,  $p=0.012$ , one-sample t-test, for statistics see **Supplementary file 7**) and this inhibition was slowly reversible. (A)  $I_{Ca}$  before (black), during (red) and after (blue) SNX-482 application. (B) Example of peak  $I_{Ca}$  plotted over time during SNX-482 application. The asterisks mark the time points of the recordings shown on the left. Single depolarizing voltage steps to  $0$  mV were applied from a holding potential of  $-60$  mV every  $10$  s. (C) Mean effect of SNX-482 on peak  $I_{Ca}$ . \*,  $p<0.05$  ( $n=8$ ; two-tailed paired t-test). (D) Remaining peak  $I_{Ca}$  after SNX-482 inhibition. \*,  $p<0.05$  (two-tailed one sample t-test). Box plots: Whiskers indicate minimal and maximal values, '+'-sign: mean, horizontal line: median. No complete concentration-response curves were generated since higher concentrations of SNX-482 are known to also inhibit other Cav channels (Bourinet et al., 2001; Newcomb et al., 1998). Therefore, our experiments may underestimate the overall contribution of Cav2.3 channel to total  $I_{Ca}$ , also because a fraction of channels must already be inactivated at the selected holding potential ( $-60$  mV) of these experiments. (E–H) Under identical experimental conditions, nifedipine reduced  $I_{Ca}$  to  $90\% \pm 1.4\%$  of control ( $p=0.031$ , Wilcoxon-test, for statistics see **Supplementary file 7**), and this inhibition was fully reversible. (E) Perforated patch-clamp recording of  $I_{Ca}$  before (black), during (red) and after (blue) nifedipine application. (F) Example of peak  $I_{Ca}$  plotted over time during nifedipine application. The asterisks mark the time points of the recordings shown on the left. Single depolarizing voltage steps to  $-10$  mV were applied from a holding potential of  $-60$  mV every  $10$  s. (G) Mean effect of nifedipine on peak  $I_{Ca}$ . \*,  $p<0.05$  ( $n=6$ ; two-tailed paired t-test). (H) Remaining peak  $I_{Ca}$  under nifedipine.  $p<0.05$  (two-tailed Wilcoxon signed-rank test). Box plots: Whiskers indicate minimal and maximal values, '+'-sign: mean, horizontal line: median. For statistics see **Supplementary file 7**. (I) Current-clamp recording of a DA neuron in the SN pars compacta to demonstrate the pre-identifying electrophysiological properties including sag potential during hyperpolarization, broad action potentials, and regular pacemaking. Arrowhead: largely reduced slow afterhyperpolarization due to partial block of  $K^+$  channels by  $Cs^+$  diffusion into the neuron during the perforation process. (J) Post-recording analysis shows co-localization of biocytin (recorded neuron; magenta) and tyrosine hydroxylase (TH, green).1

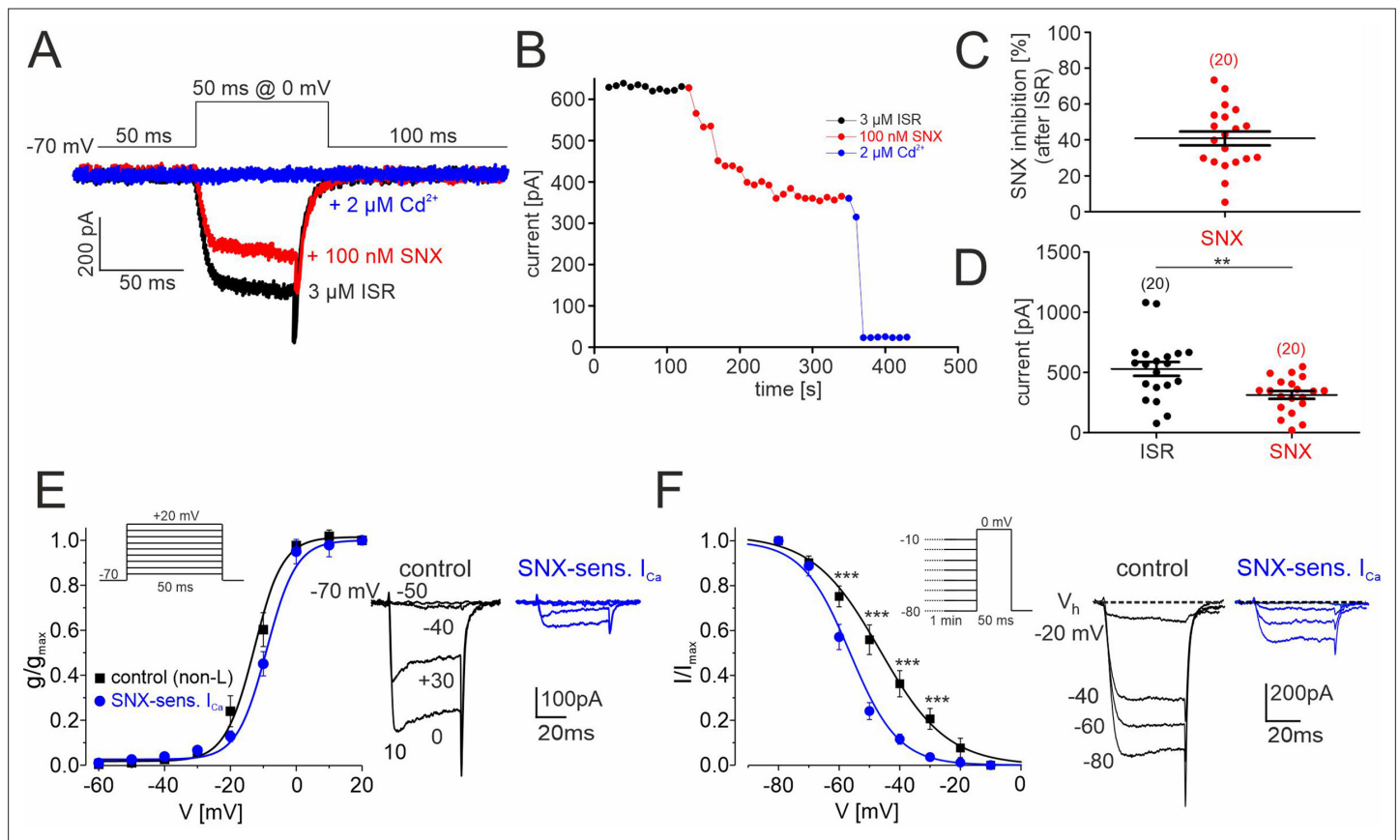


**Figure 7.** SNX-482-sensitive R-type currents in cultured mouse midbrain DA neurons. **(A)** Representative traces illustrating the inhibition of non-L-type  $I_{Ca}$  by 100 nM SNX-482 (red). Cells were initially perfused with a bath solution containing 3  $\mu$ M isradipine (black). Full block was obtained using 2  $\mu$ M  $Cd^{2+}$  (blue). Square pulses (50 ms) were applied to 0 mV from a holding potential of  $-70$  mV (top) **(B)** Current amplitude values plotted as a function of time. After stabilization of  $I_{Ca}$  with ISR (black circles), 100 nM SNX-482 was applied. The remaining currents was blocked by 2  $\mu$ M  $Cd^{2+}$ . Current run-down in the absence of drugs during 150 s was less than 1% ( $0.48 \pm 0.18\%$ ;  $n=4$  cells). **(C)** SNX-482 inhibition expressed as % of control  $I_{Ca}$  after LTCC block using 3  $\mu$ M ISR. **(D)** Mean current amplitude at the end of ISR application and at the end of SNX-482 application. Absolute current amplitude decreased from  $529 \pm 57$  pA (95% CI: 409–649) to  $313 \pm 33$  pA (95% CI: 245–381,  $n=20$ ,  $p<0.01$ , paired Student's t-test). Data represent the means  $\pm$  SEM for the indicated number of experiments ( $N=4$ ). Statistical significance was determined using paired Student's t-test: \*\*\*  $p<0.001$ ; \*\*  $p<0.01$ ; \*  $p<0.05$ . **(E)** Left: Depolarizations of 50 ms were repeated every 10 s to the indicated potentials from a holding potential of  $-70$  mV (inset). The voltage dependence of the conductance,  $g(V)$ , was calculated with the equation  $g(V) = I_{Ca}/(V - E_{Ca})$  with  $E_{Ca} = +65$  mV for the currents recorded in the presence of 3  $\mu$ M ISR (control; black squares;  $n=9$ –14 per voltage) and after subtraction of the currents insensitive to 100 nM SNX-482 ( $n=4$ –7) to yield (SNX-sensitive R-type; blue circles). Data were fitted to a Boltzmann function. At each test potential ( $V$ )  $I_{Ca}$  was estimated at the peak of the current trace. Right: representative current traces recorded during pulses to  $-50$ ,  $-40$ ,  $-30$  and 0 mV. **(F)** Left: To determine the voltage-dependence of steady-state inactivation, test pulses of 50 ms to 0 mV were preceded by 1 min prepulses to voltages from  $-80$  to  $-10$  mV. This stimulation protocol (inset) was better tolerated by cultured DA midbrain neurons than the classical protocol used previously with other cells (Calorio et al., 2019; Pinggera et al., 2015). SNX-sensitive R-type currents (blue) were obtained after subtraction of the currents insensitive to 100 nM SNX-482 ( $n=3$ –8 per voltage) from non-L control current (black,  $n=8$ –15). Right: representative traces recorded at 0 mV from a holding potential of  $-20$ ,  $-40$ ,  $-60$ , and  $-80$  mV. Inactivation curves could be best fit to Boltzmann functions with the following parameters: R-type:  $V_{0.5, inact} = -58.1 \pm 0.6$  mV,  $k = -7.1 \pm 1.2$  mV; control:  $V_{0.5, inact} = -48.0 \pm 0.9$  mV,  $k = -11.1 \pm 1.2$  mV. The R-type currents (**E**, **F**) appear smaller than expected from the data in panels B and C (30–40% of non-L-type currents). This is due to a run-down of SNX-sensitive current during the repeated depolarizations used to determine the voltage-dependence of gating. This has only minimal effects on gating parameters. When accounting for a linear run-down of 40%, the  $V_{0.5, act}$  would shift only from  $-58$  to  $-56$  mV. Source data provided in

Figure 7—source data 1.



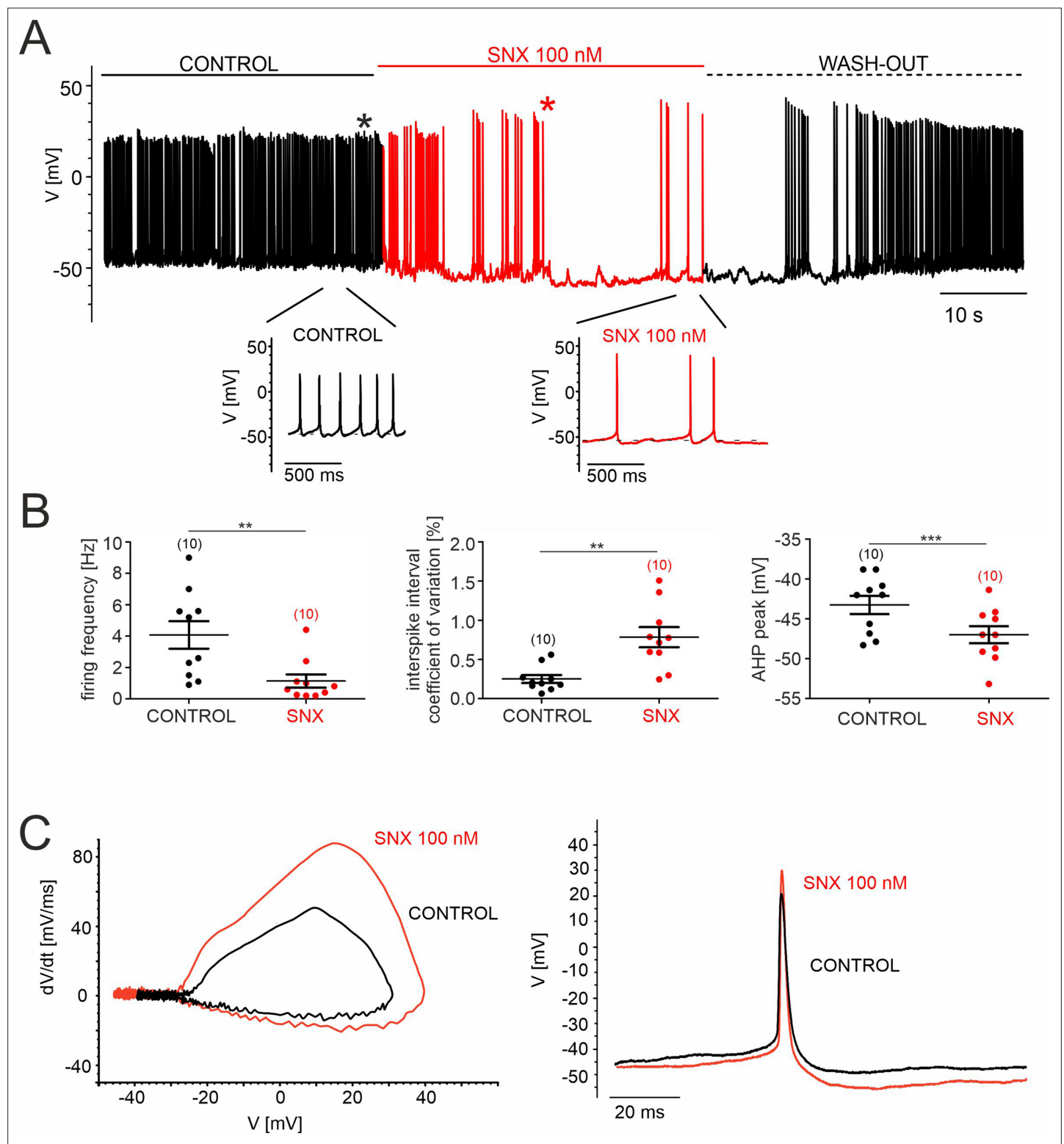


**Figure 7—figure supplement 1.** SNX-482 effects on pacemaking of cultured mouse midbrain DA neurons. (A) Representative recording of spontaneous firing activity of cultured midbrain dopaminergic neurons before, during and after the application (wash-out) of 100 nM SNX-482. Below, enlargements of action potentials within the highlighted regions are shown. (B) Firing frequency [Hz], coefficient of variation of the interspike interval [%], and AHP peak [mV] before (control) and during the application of 100 nM SNX-482. Data represent the means  $\pm$  SEM for the indicated number of experiments. Statistical significance was determined using paired Student's t-test.: \*\*\*  $p < 0.001$ ; \*\*  $p < 0.01$ ; \*  $p < 0.05$ . (C) Left panel: Phase-plane plot analysis (time derivative of voltage (dV/dt) vs. voltage (V)) before (control) and during the application of 100 nM SNX-482. Right panel: corresponding

Figure 7—figure supplement 1 continued on next page

*Figure 7—figure supplement 1 continued*

AP trace in control and in the presence of SNX-482 (obtained from trace in panel A, as indicated by the asterisks). SNX-482 significantly reduced the spontaneous firing frequency from  $4.1 \pm 0.8$  Hz (control,  $n=10$ ,  $N=3$ ; 95% CI: 2.1–6.1) to  $1.1 \pm 0.2$  Hz (SNX-482,  $n=10$ , 95% CI: 0.2–2.1,  $p=0.0036$ , paired Student's t-test) and decreased the regularity of pacemaking coefficient of variation of the mean interspike interval increased from  $0.25 \pm 0.06$  (control, 95% CI: 0.15–0.39) to  $0.78 \pm 0.13$  (SNX-482, 95% CI: 0.49–1.09,  $p=0.0032$ , paired Student's t-test). Slowing of firing was associated with hyperpolarization of the most negative voltage reached during the afterhyperpolarization (AHP) immediately after the spike (AHP peak), which decreased from  $-43.2 \pm 1.3$  mV (control, 95% CI:  $-45.8$ – $-40.7$ ) to  $-47.0 \pm 1.2$  mV (SNX-482, 95% CI:  $-49.4$  to  $-44.6$ ,  $p=0.0005$ , paired Student's t-test). Other changes in the AP waveform, which could represent indirect effects from the slowing of AP frequency or result from inhibition of Cav2.3 channels, were also noted: a reduced mean AP half-width (control:  $5.1 \pm 0.3$  ms, 95% CI: 4.4–5.8; SNX-482:  $4.2 \pm 0.3$  ms, 95% CI: 3.7–4.8;  $p=0.0050$ , paired Student's t-test), and a trend toward increased maximum time-derivative of voltage (control:  $45.3 \pm 4.9$  mV/ms, 95% CI: 34.4–56.3; SNX-482:  $74.3 \pm 13.5$  mV/ms, 95% CI: 47.0–101.5,  $p=0.0625$ , paired Student's t-test, estimated from the phase-plane plot of in C). The latter is likely due to the recruitment of more voltage-gated  $\text{Na}^+$ -channels during the AP onset from the more hyperpolarized interspike membrane potential (Guarina et al., 2018; Tomagra et al., 2019). Source data provided in **Figure 7—figure supplement 1—source data 1**.